PAPER

Check for updates

The effect of Ti-doping on the electrochemical activity of the Li$_{0.44}$MnO$_2$ cathode material for Li-ion batteries

Jaya Yadav, [ID] [a] Sai Pranav Vanam,[a] Shubham K. Parate,[b] Nikhil Doddi,[a] Velaga Srihari,[c] Valérie Pralong, [ID] [de] Maximilian Fichtner [ID] [fg] and Prabeer Barpanda [ID] *[afg]

Manganese-based oxides can function as economical cathode materials for Li-ion batteries. Various metastable manganese oxides can exhibit efficient Li$^+$ (de)insertion activity. One such system is chemically derived Li$_{0.44}$MnO$_2$ offering reversible Li$^+$ intercalation involving the Mn^{4+}/Mn^{3+} redox reaction albeit with poor rate kinetics. In this work, the electrochemical activity of tunnel-structured Li$_{0.44}$MnO$_2$ has been enhanced by tailoring its crystal structure and particle morphology by Ti-doping into Mn sites. X-ray diffraction and spectroscopy analyses revealed successful Ti-doping while retaining the original structure. Varying degrees of Ti-doping were found to exhibit improved electrochemical performance, with Li$_{0.44}$Mn$_{0.89}$Ti$_{0.11}$O$_2$ delivering the highest capacity of 129 mAh g^{-1} at a rate of C/20. Ti-doping was further found to improve the Li$^+$ diffusivity and rate kinetics. This enhancement in electrochemical activity can be ascribed to the combined effect of Ti-induced lattice expansion and decrease in particle size. Electrochemical titration and *ex situ* analyses revealed the occurrence of a single-phase (solid-solution) redox mechanism. Ti-doped Li$_{0.44}$MnO$_2$ can be harnessed as an economical cathode for Li-ion batteries.

1. Introduction

Since their commercialization in the 1990s by SONY®, Li-ion batteries are being widely used in sectors ranging from a variety of small-scale consumer electronics to large-scale (hybrid) electric vehicles and grid storage. Cathodes are key components governing the net cost and performance of batteries, thus driving the exploration of design and development of efficient cathode frameworks. While Co- and Ni-based oxides rule the commercial battery sector, there is a growing need to develop low-cost cathodes from earth-abundant elements (like Fe or Mn). Mn-based oxides are particularly attractive due to their large number of advantages in terms of less toxicity, tunable redox potential owing to variable oxidation states, and structural diversity/polymorphism.[1,2]

Bruce *et al.* reported one such composition, LiMnO$_2$ layered oxide, delivering a high initial capacity of >200 mAh g^{-1} even at a high current density of 0.5 mA cm^{-2}. However, the capacity retention was poor during cycling.[3] Other than layered oxides, spinel-structured LiMn$_2$O$_4$ has also been exploited as a cathode, but suffers from fast capacity decay at elevated temperatures (*ca.* $T > 55$ °C) in acidic electrolytes.[4] Armstrong *et al.* reported Li$_x$MnO$_2$ possessing a tunnel structure with excellent capacity retention in the voltage window of 2.8–3.6 V, but the capacity was limited to 80–85 mAh g^{-1} at a current density of 0.5 mA cm^{-2}. In contrast to spinel LiMn$_2$O$_4$, this material showed remarkable cyclability at a high temperature of 85 °C and without any layer-to-spinel phase transformation unlike many layered oxides.[5,6] Glycine-nitrate combustion synthesized Li$_x$MnO$_2$ (GNP-Li$_x$MnO$_2$) demonstrated better rate capability than solid-state synthesized Li$_x$MnO$_2$ (SS-Li$_x$MnO$_2$).[6] Despite numerous attempts to improve the electrochemical activity of Li$_{0.44}$MnO$_2$ *via* different synthesis techniques and structural modification, additional enhancements are needed to ensure its suitability for potential applications. Also, Mn-based cathode materials suffer from Jahn–Teller distortion, which affects

[a] *Faraday Materials Laboratory (FaMaL), Materials Research Center, Indian Institute of Science, Bangalore 560012, India. E-mail: prabeer@iisc.ac.in*

[b] *Centre for Nano Science and Engineering (CeNSE), Indian Institute of Science (IISc), Bangalore 560012, India*

[c] *Synchrotron Utilization Section, Raja Ramanna Centre for Advanced Technology, Indore 452013, India*

[d] *Normandie University, ENSICAEN, UNICAEN, CNRS, CRISMAT, Caen 14000, France*

[e] *Réseau sur le Stockage Electrochimique de l'Énergie (RS2E), Amiens, France*

[f] *Helmholtz Institute Ulm (HIU), Electrochemical Energy Storage, Ulm 89081, Germany*

[g] *Institute of Nanotechnology (INT), Karlsruhe Institute of Technology (KIT), Karlsruhe 76021, Germany*

their cycling stability. Ion substitution has been proven to be an efficient strategy to enhance the electrochemical properties in terms of capacity, cycling stability, rate performance, and preventing phase transformations by tuning the crystal structure.[7–9] For example, substituting Li with Ca increased capacity retention.[10] Similarly, partial substitution of Mn with Ti was found to enhance long-term capacity retention and to mitigate material dissolution.[11–13] A two-fold increase in capacity was observed when additional lithium was inserted *via* molten $LiNO_3$–LiOH at a low temperature.[14] Hence, tunnel-structured Li_xMnO_2 forms a promising compound for low-cost energy storage applications.

Li_xMnO_2, with a tunnel-type crystal structure, has five different crystallographic Mn sites, with MnO_6 octahedra and MnO_5 polyhedra forming two types of tunnels. Li1 resides in the pseudohexagonal smaller tunnel, while Li2 and Li3 occupy larger S-shaped tunnel sites.[5] To date, studies on Li_xMnO_2 systems have been mostly conducted in the voltage window of 2.5–4.8 V. But, high voltage (*ca.* >4.6 V) cycling is usually associated with electrolyte degradation or triggering of anion redox, resulting in large voltage hysteresis and rapid capacity fading when carbonate electrolytes are used.[15,16] The electrochemical performance of tunnel structured Li_xMnO_2 can be improved with Ti substitution that involves multiple factors including the synthesis protocols, cell configuration, structural modification, appropriate electrolyte, *etc.*[17] Herein, we have tuned the degree of Ti-substitution and operational window to obtain chemically derived $Li_{0.44}Mn_{1-x}Ti_xO_2$ with optimum electrochemical performance. The role of Ti-substitution in lattice modification and diffusion rate kinetics has been investigated along with the underlying solid-solution redox mechanism upon Li^+ (de)insertion.

2. Experimental

2.1. Material synthesis

Pristine and Ti-doped $Li_{0.44}Mn_{1-x}Ti_xO_2$ (*x* = 0, 0.11, 0.22, 0.33, 0.44, and 0.56) powders were obtained by conventional solid-state synthesis of their Na analogues followed by Na–Li ion-exchange involving molten salt.[12] First, stoichiometric amounts of $NaNO_3$ (99.7%, Sigma), $MnCO_3$ (99%, Alfa Aesar), and TiO_2 (99.8%, Alfa Aesar) were thoroughly mixed for 20 minutes using an agate mortar and pestle. These precursor mixtures were calcined at 900 °C for 6 h (heating rate = 5 °C min^{-1}) in a muffle furnace (in air) to yield $Na_{0.44}Mn_{1-x}Ti_xO_2$ (*x* = 0, 0.11, 0.22, 0.33, 0.44, and 0.56) products. A starting ratio of Na/(Mn + Ti) = 0.5 was taken to compensate for Na loss at high temperature. Then, the ion exchange reaction was carried out by mixing the Na-based $Na_{0.44}Mn_{1-x}Ti_xO_2$ oxides with a eutectic combination of $LiNO_3$ (88 mol%) and LiCl (12 mol%), which was calcined at 300 °C for 10 h (heating rate = 5 °C min^{-1}) in a muffle furnace (in air) to obtain the target $Li_{0.44}Mn_{1-x}Ti_xO_2$ compounds.

2.2. Material characterization

The crystal structure was characterized by X-ray powder diffraction with a PANalytical X'pert Pro diffractometer equipped with

a Cu Kα source (λ_1 = 1.5405 Å, λ_2 = 1.5443 Å) operating at 40 kV/30 mA. The diffractograms were collected in the 2θ range of 5–80° with a scanning step of 0.026° in Bragg–Brentano geometry. Synchrotron XRD patterns were acquired at the BL-11 beamline at the Indus-2 synchrotron facility (Raja Ramanna Centre for Advanced Technology, Indore, India) with a beam wavelength of 0.7305 Å. Rietveld refinement was performed using the FullProf suite program.[18] Linear interpolation and pseudo-Voigt functions were used for the background and shape fitting, respectively. The crystal structure was illustrated with the VETSA software.[19]

The particle morphology was examined using high-resolution scanning electron microscopy (Ultra 55 FESEM Carl Zeiss EDS, operating at 5–20 kV) and transmission electron microscopy (Thermo Fisher Titan Themis, operating at 300 kV). X-ray photoelectron spectroscopy surface analysis was carried out with a Thermo Scientific K_α XPS instrument with an incident monochromated X-ray beam from the Al target (accelerating voltage = 12 kV and emission current = 6 mA). Shift corrections were done by taking carbon as the reference at a binding energy of 284.6 eV. Magnetic susceptibility was measured with a Quantum Design MPMS XL SQUID magnetometer in a DC field in the temperature range of 2–400 K in zero-field-cooled (ZFC) mode. Fourier-transform infrared (FTIR) spectroscopy was conducted with a PerkinElmer (Frontier) instrument using transmission mode in the wavenumber window of 400–7800 cm^{-1}. Raman spectra were acquired with a LabRAM HR unit (Horiba Jobin Yvon) using a 532 nm (green) laser as the excitation source.

For post-mortem analysis, the samples were recuperated at different states of (dis)charge during electrochemical cycling at a rate of C/40. The cathodes were cycled using coin-type (CR-2032) or Swagelok cells as described below. Afterwards, the cells were disassembled and the electrodes were washed with propylene carbonate and dried before various material characterization studies.

2.3. Electrochemical characterization

The working electrodes were prepared by thoroughly mixing the as-synthesized active material, super P-carbon black, and polyvinylidene fluoride (PVDF) in proportions of 80 : 10 : 10 (w/w/w) in *N*-methyl-2-pyrrolidone (NMP). This slurry was coated uniformly on Al foil using a doctor blade and was dried at 80 °C overnight in a vacuum oven. The active mass loading was 2–4 mg cm^{-2}. CR2032 type coin cells were assembled in an Ar-filled glovebox (MBraun LABstar glovebox with a H_2O/O_2 level of <0.5 ppm). Metallic Li foil was used as counter and reference electrodes for the Li-ion half-cells. The separation between working and counter electrodes was maintained by a glass microfiber filter (Whatman, grade GF/C) saturated with a commercial electrolyte comprising 1 M $LiPF_6$ in ethylene carbonate (EC)/diethyl carbonate (DEC)/dimethyl carbonate (DMC) (1 : 1 : 3 (v/v/v)) (Sigma Aldrich). Galvanostatic (dis)charge tests were conducted in the voltage window of 2–4 V (*vs.* Li^+/Li) (at 25 °C) using a Neware BTS-4000 battery tester. Cyclic voltammetry (CV) at different scan rates (from 0.1–1 mV s^{-1}), the

potentiostatic intermittent titration technique (PITT) at a rate of C/50 and the galvanostatic intermittent titration technique (GITT) at a rate of C/20 were performed using a Bio-Logic BCS 805/810 automatic battery cycler. Electrochemical impedance spectroscopy (EIS) was performed in the frequency range of 10 mHz–200 kHz using a Bio-Logic SP300 workstation.

3. Results and discussion

While the solid-state route often yields thermodynamically stable polymorphs/phases, numerous soft chemistry methods (involving two or more steps) can be adopted to stabilize various metastable (intermediate) phases often exhibiting superior material properties and performance. The layered structured LiT_MO_2 (T_M = 3d metals) oxides can be obtained by direct high-temperature synthesis. On the other hand, the formation of tunnel structured Li_xMnO_2 needs a two-step soft chemistry protocol. Here, the target pristine and Ti-doped $Li_{0.44}Mn_{1-x}Ti_xO_2$ (x = 0, 0.11, 0.22, 0.33, 0.44, and 0.56) phases were prepared by molten salt ion-exchange using their Na-analogues as starting materials.[12] The scheme for this two-step synthesis is depicted in Fig. 1a. With a higher degree of Ti-doping, the colour of powder samples changed from black to brown. The phase purity of pristine $Li_{0.44}MnO_2$ (now onwards referred to as LMO1) was verified by Rietveld refinement of synchrotron XRD patterns (Fig. S1). Phase-pure LMO1 was obtained assuming an orthorhombic crystal structure with *Pbam* symmetry. The detail lattice parameters and lattice coordinates are given in Table S1. Then, the diffraction patterns of various Ti-doped samples were analyzed. As shown in Fig. 1b, all major diffraction peaks of all compositions can be indexed to the orthorhombic crystal system (isostructural to LMO1). A minor amount of Mn_2O_3 peaks was also observed, which is a thermodynamically stable phase.[20,21] When the Ti concentration was over 0.22, it led to the formation of a minor amount of $Li_2Ti_6O_{13}$ impurity phase.[22] The higher degree of Ti-doping led to shifting of XRD peaks to lower 2θ values, indicating the steady rise in d-spacing (*i.e.* lattice expansion). The typical crystal structure of this tunnel type oxide is illustrated in
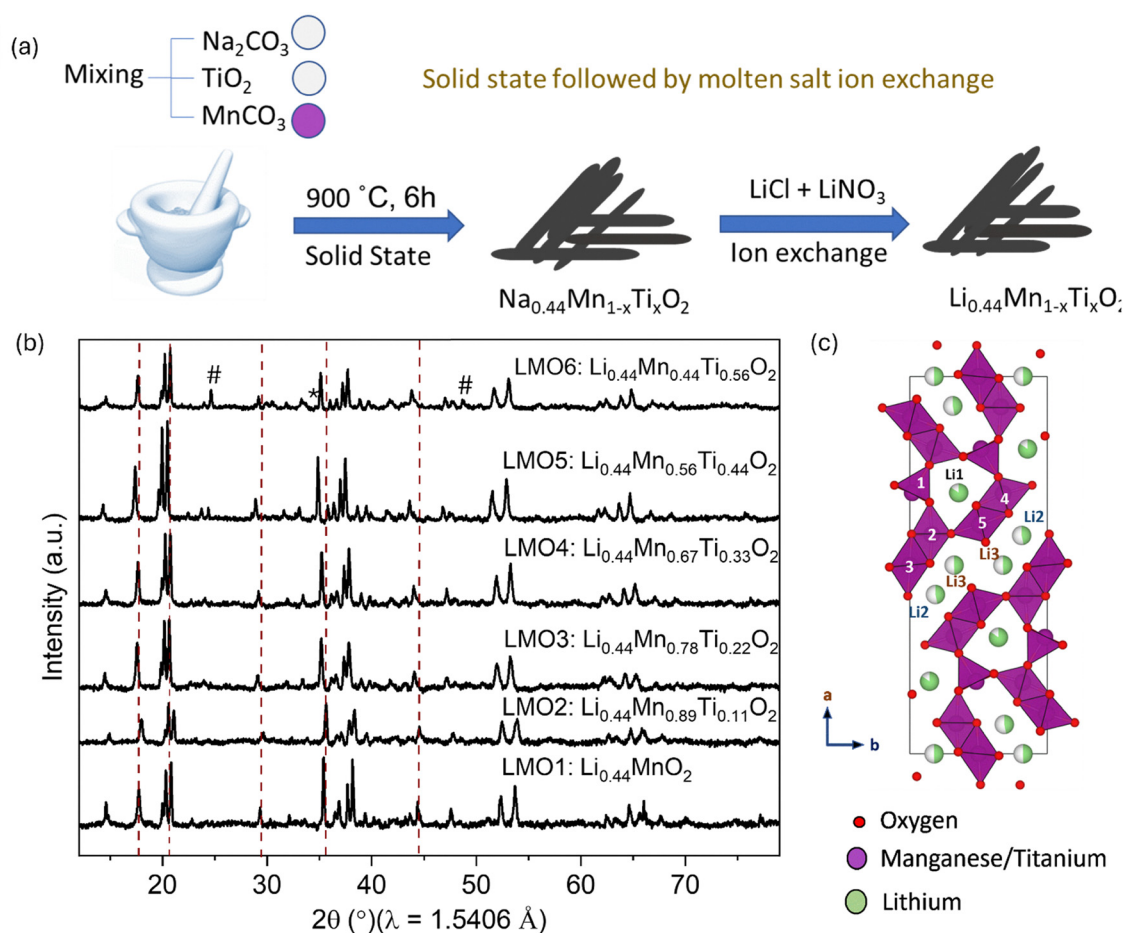

Fig. 1 (a) Scheme for the material synthesis involving the solid-state route followed by molten salt ion exchange. (b) Comparative XRD patterns of tunnel-type $Li_{0.44}Mn_{1-x}Ti_xO_2$ ($0 \leq x \leq 0.56$) oxide compositions. The vertical dashed lines are shown as a guide to the eye to illustrate steady peak shifting upon Ti-doping (*Mn_2O_3, #$Li_2Ti_6O_{13}$). (c) Structural illustration of $Li_{0.44}Mn_{1-x}Ti_xO_2$ oxide involving large tunnels. The constituent MO_6 octahedra and MO_5 polyhedra (M = Mn/Ti) are shown in pink delimiting tunnels accommodating partially occupied Li sites (green/white spheres). Constituent Mn occupies 5 distincts sites as indicated by numbers inside pink polyhedra.

Paper

Fig. 1c. There are 5 crystallographically distinct Mn sites with different oxidation states. While Mn1 and Mn2 are in the +3 oxidation state, the rest (Mn3, Mn4 and Mn5) are in the +4 oxidation state.

The size of the Ti^{4+} ion is 0.68 Å, which is comparable to that of the isovalent Mn^{4+} ion (0.60 Å).[11] Hence upon doping, Ti^{4+} most likely occupies the Mn^{4+} sites (at a low concentration of Ti). Even with a higher degree of Ti doping, Ti^{4+} does not enter Mn1 sites having square pyramidal geometry.[23] To probe the sites occupied by Ti, the synchrotron XRD study was conducted for $Li_{0.44}Mn_{0.89}Ti_{0.11}O_2$ (here onwards referred to as LMO2). The corresponding Rietveld refinement and crystal structure are shown in Fig. 2. The lattice parameters and coordinates are listed in Tables S2 and S3. Ti was found to majorly occupy Mn4 and Mn5 sites as illustrated in Fig. 2b, which led to the expansion in lattice parameters and unit cell volume (Table S3).

In addition to diffraction, magnetic properties can be gauged for detecting structural defects and compositional changes in battery materials containing 3d transition elements. Fig. 2c compares the magnetic susceptibility behaviour of the pristine (LMO1) and Ti-doped $Li_{0.44}Mn_{0.89}Ti_{0.11}O_2$ (LMO2) and $Li_{0.44}Mn_{0.44}Ti_{0.56}O_2$ (LMO6) compositions. In the case of pristine LMO1, a clear paramagnetic to antiferromagnetic transition was observed at around $T_N \sim 9$ K. However, upon Ti^{4+} doping into the structural framework, the replacement of Mn^{4+}/Mn^{3+} ions by the nonmagnetic Ti^{4+} ion (which has a d^0 configuration) decreased the exchange interactions between $Mn^{4+}–O–Mn^{4+}/Mn^{3+}$.[24,25] Thus, upon gradual Ti-doping, a decrease in antiferromagnetic exchange interactions was noticed with no sharp transition points. This further attests successful Ti-doping into the lattice framework. Then, the presence of Ti was probed using XPS spectroscopy. Fig. 2d
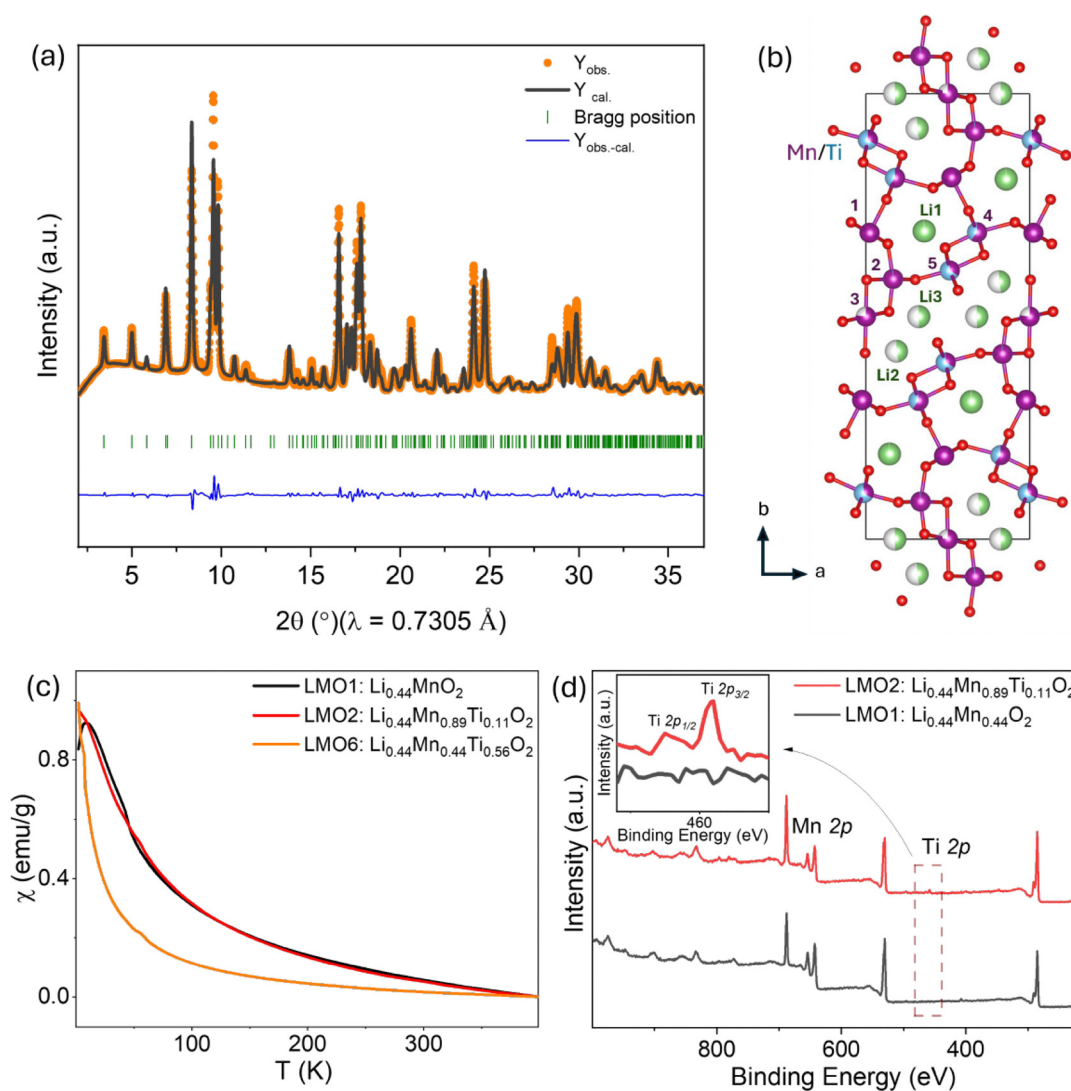
Fig. 2 (a) Rietveld refined synchrotron XRD pattern (λ = 0.7305 Å) of $Li_{0.44}Mn_{0.89}Ti_{0.11}O_2$ (LMO2). The experimental data points (yellow dots), simulated pattern (black line), their difference (blue line) and Bragg diffraction peaks (green ticks) are shown. (b) The corresponding crystal structure is shown comprising Mn/Ti octahedra (Mn in purple and Ti in blue spheres) and Li (green spheres). (c) Comparative magnetic susceptibility plots of LMO1, LMO2 and LMO6. (d) Wide XPS survey spectra of pristine (LMO1) and Ti-doped $Li_{0.44}MnO_2$ (LMO2) (the inset displays the Ti 2p peak in LMO2).

shows the wide range core-level XPS survey spectra of LMO1 and LMO2. A characteristic Ti 2p peak was observed in LMO2, which was absent in the case of LMO1. Furthermore, FTIR spectra of different Ti-doped compositions are illustrated in Fig. S2. In addition to the bands related to Mn–O and Mn–O–Mn stretching/bending modes, the gradual doping of Ti led to the appearance of peaks corresponding to O–Ti–O bending and Ti–O asymmetric stretching.[26] Overall, Ti-doping was confirmed using various diffraction and spectroscopy tools.

The ion-exchange produced LMO1 with a rod-like micrometric morphology oriented along the c-direction (Fig. 3a and b). The corresponding HRTEM and SAED patterns revealed its crystalline nature. Uniform elemental distribution was captured by HAADF-STEM elemental mapping as shown in Fig. S3. LMO2 also exhibited a morphology with rods growing along the [001] direction (Fig. 3e and f). Uniform Ti-doping was revealed by elemental mapping with the expected atomic fraction (Fig. S4). The diffraction spots observed in the SAED pattern (Fig. 3g) confirmed the tunnel-type orthorhombic structure. From HRTEM images, an increase in the d-spacing of the (200) plane was observed for LMO2 (0.4493 nm) as compared to LMO1 (0.4438 nm) (Fig. 3d and h). All Ti-doped oxide samples had a similar morphology (Fig. S5). However, upon gradual increase in the Ti concentration, the length of the rods along the c-direction became shorter. Following successful synthesis, the effect of Ti-doping on electrochemical activity was investigated.

The galvanostatic (dis)charge capacity of all Ti-doped compositions was evaluated using the as-synthesized active materials without any further cathode optimization. The corresponding profiles of cells, cycled in the potential window of 2–4 V (at a C/20 rate), are shown in Fig. 4 and Fig. S6. The respective differential voltage (dQ/dV) profiles are given in Fig. S7. The pristine $Li_{0.44}MnO_2$ exhibited a multistep voltage profile involving Mn^{4+}/Mn^{3+} redox activity centered at 3.2 V

(vs. Li/Li^+). Ti-doping led to an increase in capacity for LMO2 exhibiting the highest first discharge capacity of 128 mAh g^{-1}. This increase in electrochemical activity can be attributed to the ease of Li^+ (de)intercalation owing to Ti-induced structural expansion. While Li^+ (de)insertion primarily occurs from larger Li2 and Li3 sites (Fig. 1c), upon Ti-doping, the Li1 site can become accessible due to lattice expansion. Hence, LMO2 exhibited enhanced capacity. The higher degree of Ti-doping led to a steady decrease in capacity (Fig. S6) due to the lower amount of electroactive species (Mn^{4+}). Also, the voltage profiles became slopier with progressing Ti doping with the average redox activity centered around 3.2 V.

A comparison of the rate performance of LMO1 and LMO2 is displayed in Fig. 4c. The Ti-doped LMO2 delivered reversible capacities of 129.4, 115.6, 98, and 73 mAh g^{-1} at C/20, C/10, C/5 and C/2, respectively, which were higher than that of pristine LMO1 at the respective rates. The superior rate kinetics in LMO2 can be attributed to its larger lattice size stemming from Ti-doping. In addition to higher capacity and rate kinetics, Ti-doping was also found to enhance the cycling stability (Fig. 4a and b). Fast cycling was performed at a rate of 2C (Fig. 4d). LMO2 showed better capacity retention of 85.2% after 50 cycles with stable coulombic efficiency. This can be due to the decrease in the number of Jahn–Teller active Mn^{3+} species.[27] Also, the bond energy of Ti–O (662 kJ mol^{-1}) is significantly higher than that of Mn–O (402 kJ mol^{-1}). This strong Ti–O bond can stabilize the structure by mitigating substantial bond changes in the Mn^{4+}–O bond within the octahedral environment. This stabilization occurs because oxygen atoms are shared between Mn^{3+}/Mn^{4+} and Ti^{4+} during the transition metal redox process.[22] A comparison with previously reported tunnel-type and spinel manganese oxides (Table 1) highlights that this material achieves higher or comparable retention relative to other doped tunnel-type oxides, including Ca- and Ti-substituted variants. This establishes Ti^{4+} doping as an
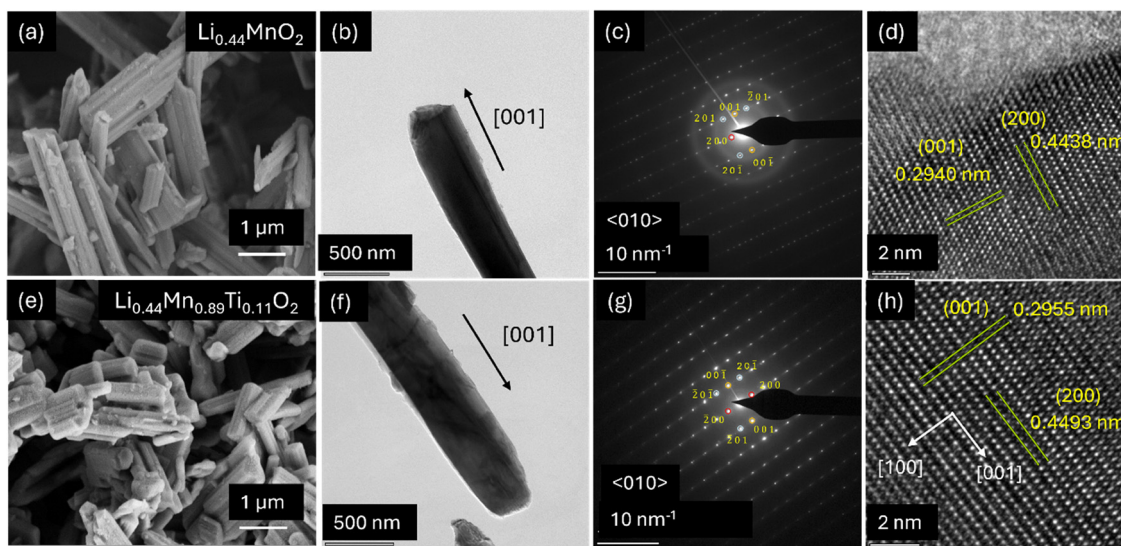

Fig. 3 Morphology analysis. (a) and (e) SEM images of $Li_{0.44}MnO_2$ (LMO1) and $Li_{0.44}Mn_{0.89}Ti_{0.11}O_2$ (LMO2). (b), (c) and (d) TEM image, SAED pattern and HRTEM image of LMO1. (f), (g) and (h) TEM image, SAED pattern and HRTEM image of LMO2. The ⟨010⟩ zone axis was taken for the SAED patterns.

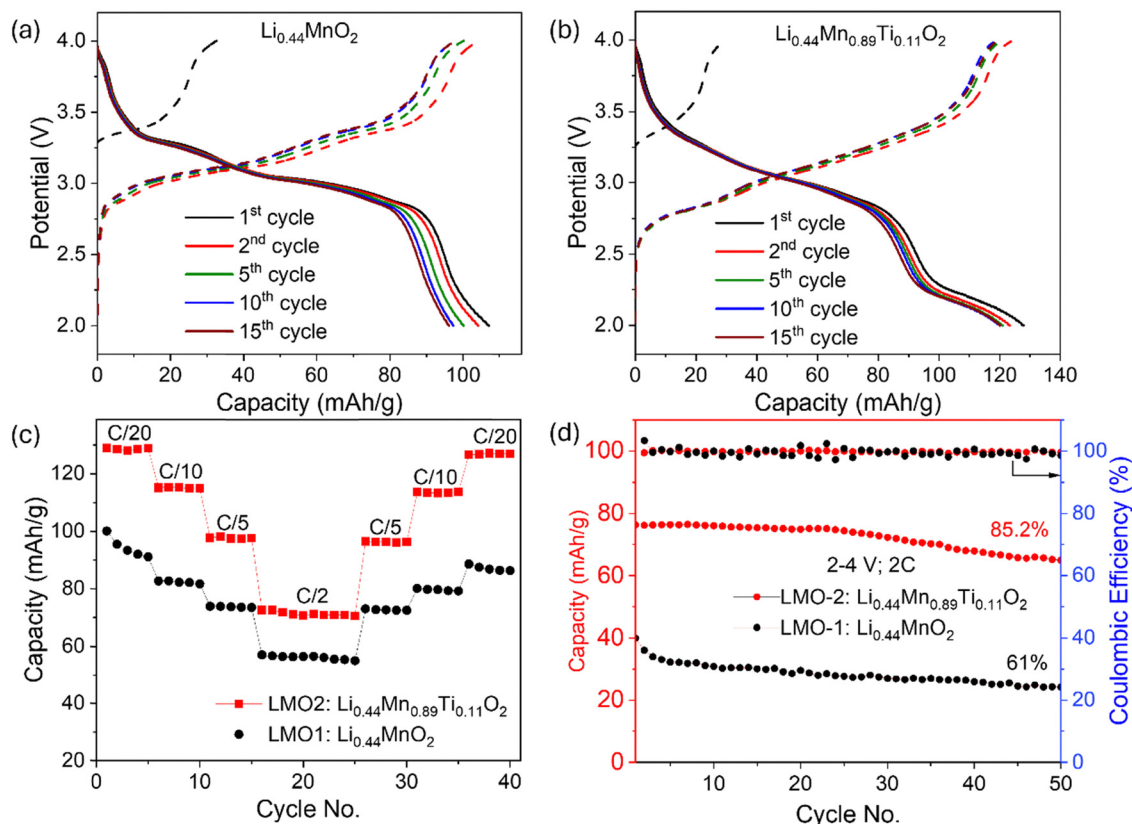**Fig. 4** Galvanostatic charge/discharge profiles for (a) pristine $Li_{0.44}MnO_2$ (LMO1) and (b) Ti-doped $Li_{0.44}Mn_{0.89}Ti_{0.11}O_2$ (LMO2) compositions cycled at a rate of C/20 (2–4 V). (c) Corresponding rate kinetics for LMO1 and LMO2. (d) Cycling stability and coulombic efficiency of LMO1 and LMO2 cycled at a fast rate of 2C in the voltage window of 2–4 V.

Table 1 Comparison of the cycling performance of Ti-doped and undoped tunnel/spinel-type Mn-based cathode materials

Material	Structure	Retention	Conditions	Ref.
$Li_{0.44}MnO_2$ (pristine)	Tunnel (*Pbam*)	~70–72% after 150 cycles	0.5 mA cm^{-2} (2–3.6 V)	5
$Na_{0.44}Mn_{0.89}Ti_{0.11}O_2$ (Ti-doped $Na_{0.44}MnO_2$)	Tunnel (*Pbam*)	~79% after 600 cycles	1C (2–3.8 V)	22
$Li_{0.27}Na_{0.007}Ca_{0.03}MnO_2$ (Ca-substituted $Li_{0.44}MnO_2$)	Tunnel (*Pbam*)	85% after 50 cycles	30 mA g^{-1} (2–4.8 V)	10
$LiMn_{1.97}Ti_{0.03}O_4$ (Ti doped $LiMn_2O_4$)	Spinel (*Fd$\bar{3}$m*)	~81.65% after 100 cycles	0.5C (2.9–4.3 V)	28
$Li_xMn_{0.89}Ti_{0.11}O_2$ (Ti-substituted $Li_{0.44}MnO_2$)	Tunnel (*Pbam*)	85.2% after 50 cycles	2C (2–4 V)	This work

effective strategy to enhance the long-term stability of tunnel-type Mn-based cathodes.

Overall, considering the optimal balance between the reversible capacity and cycling stability related to Mn^{3+} species, LMO2 was found to offer best electrochemical activity and was considered for further studies. To optimize the voltage window, the electrochemical performance was tested in different voltage windows (Fig. S8). An optimum electrochemical activity was observed within the 2–4 V window. Thus, further mechanistic studies were conducted for the LMO2 sample in the optimized voltage window of 2–4 V.

The charge compensation mechanism during Li^+ (de)insertion was analyzed by *ex situ* X-ray photoelectron spectroscopy (XPS). In the pristine LMO1, the (de)lithiation occurred involving Mn^{4+}/Mn^{3+} redox activity, as shown in Fig. S9. The *ex situ*

XPS spectra of Ti-doped LMO2 are shown in Fig. 5. The Mn 2p and Ti 2p XPS spectra were fitted using curve-fitting modes, as reported earlier.[29,30] Due to spin–orbit coupling, Mn 2p spectra split into the Mn $2p_{1/2}$ peak, centred at 653.96 eV, and the Mn $2p_{3/2}$ peak at 642.3 eV. From the deconvoluted Mn 2p spectra, Mn was found to have mixed oxidation states of Mn^{3+} and Mn^{4+}, similar to LMO1. Ti 2p split into two peaks: one peak at 463.8 eV corresponding to the Ti $2p_{1/2}$ and another peak at 458 eV corresponding to the Ti $2p_{3/2}$. This indicates the existence of the Ti^{4+} in LMO2. When LMO2 was charged to 4 V, the Mn 2p spectra still exhibited a mixed oxidation state, but with a higher ratio of Mn^{4+}/Mn^{3+}, indicating the oxidation of some Mn^{3+} to Mn^{4+} upon charging. When the LMO2 was discharged to 2 V, the Mn 2p spectra solely showed the existence of Mn^{3+}, indicating the complete reduction of Mn^{4+} to Mn^{3+} after discharge.
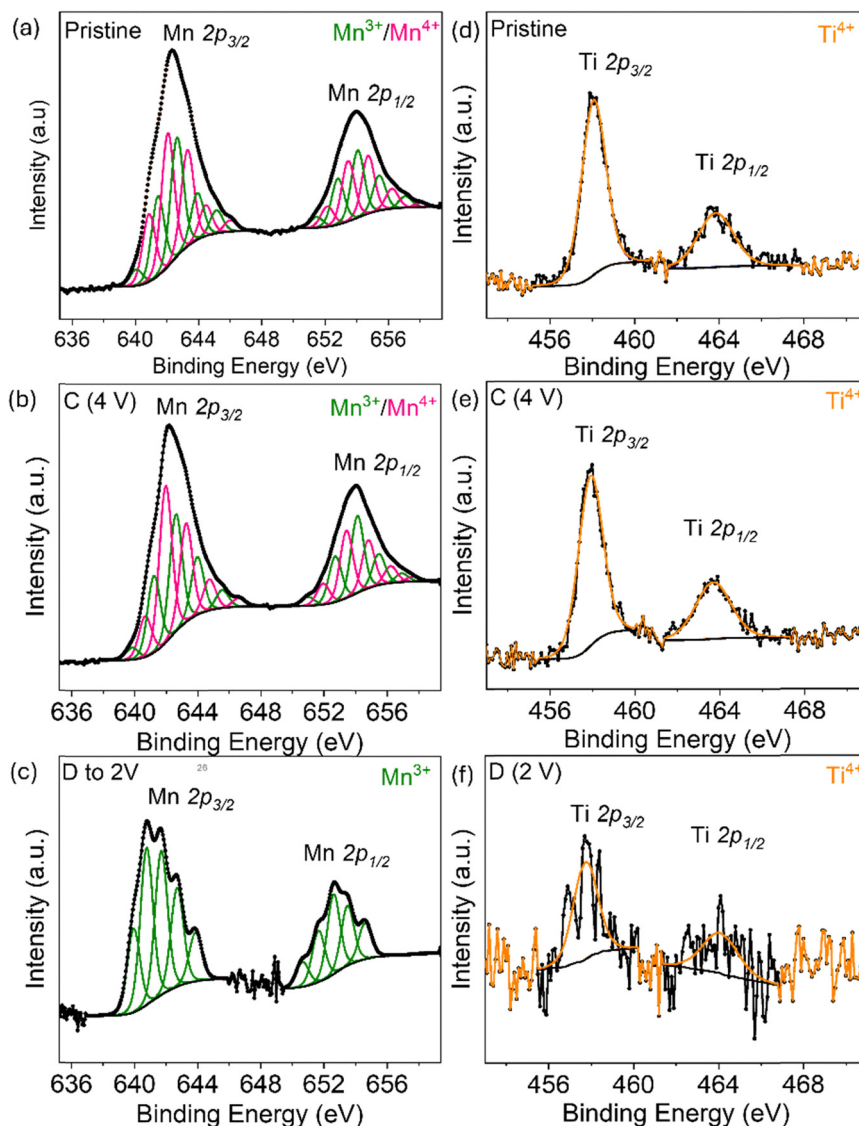
Fig. 5 Mn 2p XPS spectra of LMO2: (a) pristine cathode, (b) cathode charged to 4 V, and (c) cathode discharged to 2 V. Mn^{4+}/Mn^{3+} redox states are captured. Ti 2p XPS spectra of LMO2: (d) pristine state, (e) charged to 4 V, and (f) discharged to 2 V. The Ti^{4+} redox state remain unaltered.

The oxidation state of Ti remained unaltered ruling out any Ti redox during cycling. Hence, only Mn^{4+}/Mn^{3+} redox activity compensates for Li^+ (de)insertion.

To probe the structural evolution during cycling, *ex situ* XRD was conducted at various states of (dis)charge, as illustrated in Fig. 6a and Fig. S10. The tunnel structure with the orthorhombic crystal system was maintained at all states of charge during cycling. A small shift was observed towards the lower angle after fully discharging to 2 V, indicating lattice expansion due to more Li^+ insertion. A solid-solution redox process was confirmed without any phase transformation. Even after 1000 cycles conducted at a fast rate of 2C, the tunnel structure was maintained (Fig. S11). The reversibility of this material was observed using *ex situ* Raman spectroscopy capturing localized structural alterations (Fig. 6b). All Raman bands were unaltered after cycling. The *ex situ* TEM study was employed to probe structural evolution (Fig. 6c). Upon charging to 4 V and

discharging to 2 V, the tunnel structure and rod-like morphology were maintained within an orthorhombic crystal system. Minor changes in the *d*-spacing of planes, particularly in the (200) plane, were observed which comes back to the pristine structure upon discharging.

The Li^+ (de)insertion mechanism was thus elucidated using the potentiostatic intermittent titration technique (PITT) at a rate of C/50 in the 2–4 V range (Fig. 7a). "Cottrel-type" *I–t* behaviour was observed, indicating a monophase mechanism in accordance with the *ex situ* XRD results.[31] The rate kinetics was examined using the galvanostatic intermittent titration technique (GITT) and chemical diffusion coefficients were calculated for LMO1 and LMO2 (Fig. 7b and Fig. S12). The Ti-doped LMO2 exhibited higher diffusion coefficient values compared to LMO1, which corroborates the rate performance results. The diffusion coefficient values varied between 1.8×10^{-11}–2.08×10^{-10} and 6.367×10^{-11}–1.2×10^{-11} cm^2 s^{-1} for
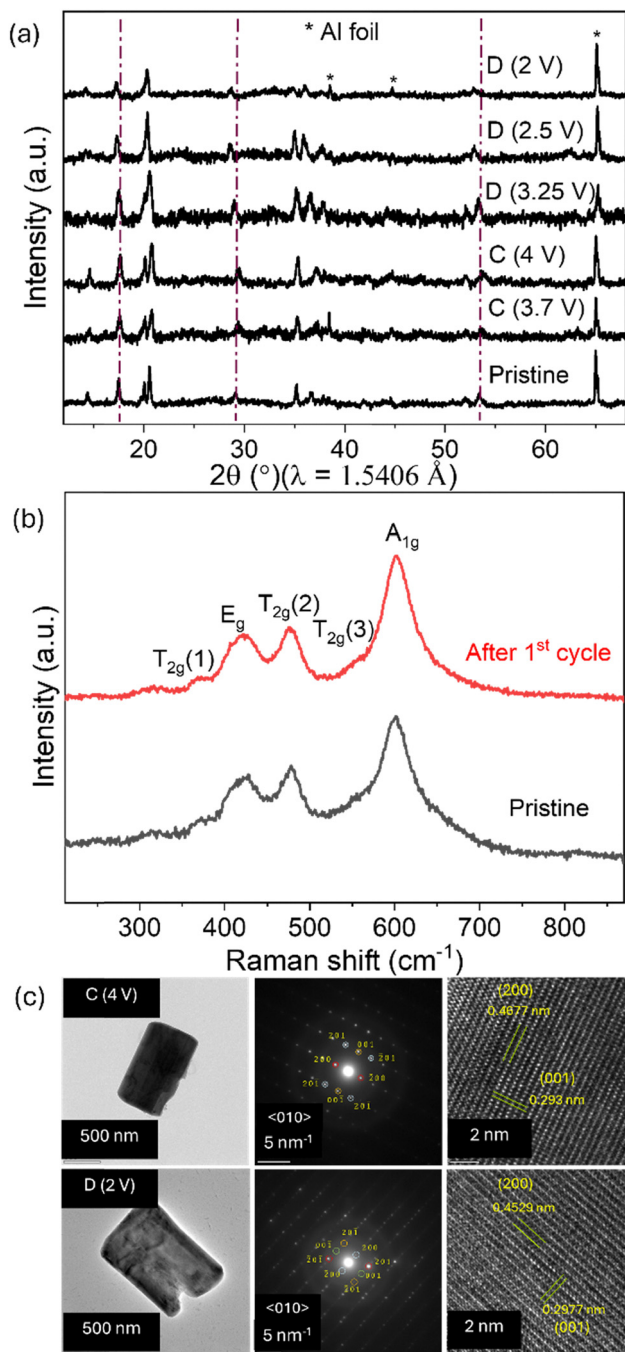
Fig. 6 (a) *Ex situ* XRD patterns of LMO2 at different states of charge. (b) Comparative Raman spectra of LMO2 in pristine and after the 1st cycle. (c) *Ex situ* TEM, SAED and HRTEM analysis of the LMO2 cathode charged to 4 V (top) and discharged to 2 V (bottom). The ⟨010⟩ zone axis was taken for the SAED patterns.
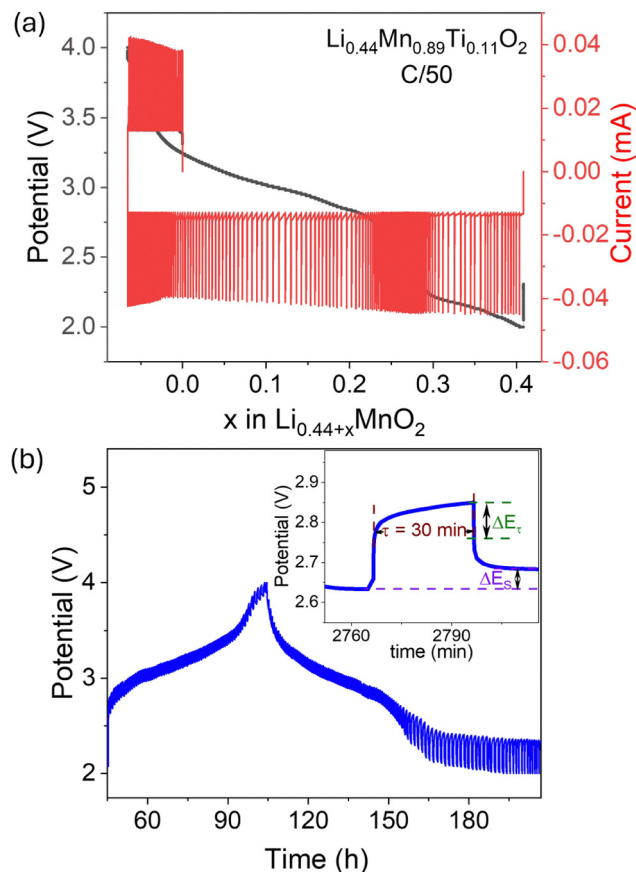

Fig. 7 (a) PITT curve of LMO2 cycled at a rate of C/50 (2–4 V). (b) Voltage profile of LMO2 during GITT (current was provided for 30 min at C/20 rate followed by rest for 1 h). The inset shows the expansion of the single titration curve.

the LMO2 and LMO1, respectively, during cycling. The diffusion coefficient values were smaller during discharge than during charge. These values fall well within the range reported by Saint *et al.* for tunnel-type Mn oxide, particularly in the voltage regime dominated by larger tunnels.[17] In addition, electrochemical impedance spectroscopy (EIS) measurements were performed after the 1st cycle (C/20) for both LMO1 and

LMO2. Nyquist plots for both undoped and Ti-doped $Li_{0.44}MnO_2$ (Fig. S13) show a typical semicircle in the high-frequency region and a sloped tail at low frequencies. The Ti-doped sample exhibits a noticeably smaller semicircle diameter, indicating reduced charge-transfer resistance (R_{ct}). This suggests improved interfacial kinetics and faster Li^+ transport. A similar trend was reported for Ti-doped $Na_{0.44}MnO_2$, where the fitting of the EIS data also revealed a decrease in R_{ct} upon Ti substitution.[8] It further affirms that Ti^{4+} enhances electrochemical performance by improving charge transport and stabilizing the electrode–electrolyte interface.[32]

The enhanced rate performance observed in the Ti-doped material can be attributed to the reduced size of rod-shaped particles, leading to higher diffusion coefficients. Here, Ti^{4+} ions are not actively engaged in electrochemical reactions within the 2–4 V range. However, their inclusion triggers an expansion in the unit cell volume, facilitating more efficient (de)intercalation of Li^+ ions. Consequently, a slight Ti doping enhances the capacity. Nevertheless, excessive Ti doping reduces the presence of electrochemically active Mn ions. Moreover, Ti^{4+} substitution at Mn^{3+} sites suppresses Jahn–Teller distortion during repeated cycling, thereby improving capacity retention. Apart from the Ti dopant concentration, the operating potential window can affect the net electrochemical

performance. To gauge the effect of the potential window, LMO2 was cycled to voltage ranging from 4.8 V to 1 V as shown in Fig. S14. The *ex situ* XPS spectra of Mn 2p and Ti 2p (at discharge to 1 V) are presented in Fig. S15. While Ti is redox inactive throughout the voltage window, extra capacity arises by triggering the Mn^{3+} to Mn^{2+} redox process at voltages below 2 V. Thus, using a wider voltage window can activate (i) anionic redox at high voltage (*ca.* >4.5 V) and (ii) multiple cationic redox (Mn^{4+}/Mn^{3+} and Mn^{3+}/Mn^{2+}) at low voltage that can yield high capacity and energy density in Ti-doped $Li_{0.44}MnO_2$ that warrants a detailed study in the future.

4. Conclusions

In summary, metastable Ti-doped $Li_{0.44}MnO_2$ compositions with an orthorhombic tunnel structure were synthesized *via* a *chimie douce* ion exchange route. A small amount of Ti-doping was found to expand the lattice in $Li_{0.44}Mn_{0.89}Ti_{0.11}O_2$, thereby activating more facile Li^+ (de)insertion. Thus, it led to an improved discharge capacity of 129 mAh g^{-1} at a rate of C/20 along with superior Li^+ diffusivity, rate kinetics and cycling stability. The charge compensation occurred *via* a solid solution (single-phase) redox mechanism. Hence, Ti-doping into tunnel-type $Li_{0.44}MnO_2$ can be adopted to improve electrochemical performance, particularly involving Jahn–Teller active Mn^{3+} species. Furthermore, by varying the operating voltage window, anionic (oxygen) redox at high voltage and multiple cationic (Mn^{4+}/Mn^{3+} and Mn^{3+}/Mn^{2+}) redox at voltages below 2 V can be exploited in these Ti-doped $Li_{0.44}MnO_2$ cathodes which will be reported shortly. Ti-doped $Li_{0.44}MnO_2$ possessing a tunnel type framework can be harnessed as an economical cathode for Li-ion batteries.

Conflicts of interest

There are no conflicts to declare.

Data availability

The data supporting this article have been included as part of the SI.

Supplementary information available: Rietveld refinement of pristine material, crystallographic details of cathode materials, FTIR spectra, elemental distribution mapping, SEM micrographs, electrochemical characterizations, XPS spectra, *ex situ* XRD patterns, GITT and EIS, *ex situ* XPS of cathodes. See DOI: **https://doi.org/10.1039/d5ma00455a**

Acknowledgements

References

1 N. Ortiz-Vitoriano, N. E. Drewett, E. Gonzalo and T. Rojo, *Energy Environ. Sci.*, 2017, **10**, 1051–1074.

2 K. Zhang, X. Han, Z. Hu, X. Zhang, Z. Tao and J. Chen, *Chem. Soc. Rev.*, 2015, **44**, 699–728.

3 P. G. Bruce, A. R. Armstrong and H. Huang, *J. Power Sources*, 1997, **68**, 19–23.

4 A. Blyr, C. Sigala, G. Amatucci, D. Guyomard, Y. Chabre and J.-M. Tarascon, *J. Electrochem. Soc.*, 1998, **145**, 194–209.

5 A. R. Armstrong, H. Huang, R. A. Jennings and P. G. Bruce, *J. Mater. Chem.*, 1998, **8**, 255–259.

6 M. M. Doeff, A. Anapolsky, L. Edman, T. J. Richardson and L. C. De Jonghe, *J. Electrochem. Soc.*, 2001, **148**, A230–A236.

7 M. Zarrabeitia, E. Gonzalo, M. Pasqualini, M. Ciambezi, O. Lakuntza, F. Nobili, A. Trapananti, A. Di Cicco, G. Aquilanti, N. A. Katcho, J. M. López del Amo, J. Carrasco, M. Á. Muñoz-Márquez and T. Rojo, *J. Mater. Chem. A*, 2019, 7, 14169–14179.

8 P. Zhan, K. Jiao, J. Wang, Z. Hu, R. Ma, H. Zhu and S. Jiao, *J. Electrochem. Soc.*, 2015, **162**, A2296–A2301.

9 G. Yang, H. Ni, H. Liu, P. Gao, H. Ji, S. Roy, J. Pinto and X. Jiang, *J. Power Sources*, 2011, **196**, 4747–4755.

10 A. Fukabori, H. Hayakawa, N. Kijima and J. Akimoto, *Electrochem. Solid-State Lett.*, 2011, **14**, A100–A103.

11 M. M. Doeff, T. J. Richardson and K. T. Hwang, *J. Power Sources*, 2004, **135**, 240–248.

12 J. Akimoto, J. Awaka, Y. Takahashi, N. Kijima, M. Tabuchi, A. Nakashima, H. Sakaebe and K. Tatsumi, *Electrochem. Solid-State Lett.*, 2005, **8**, A554–A557.

13 L. J. Hardwick, J. Saint, M. M. Doeff and R. Kostecki, *ECS Meet. Abstr.*, 2008, 718.

14 J. Awaka, J. Akimoto, H. Hayakawa and Y. Takahashi, *J. Power Sources*, 2007, **174**, 1218–1223.

15 B. Li and D. Xia, *Adv. Mater.*, 2017, **29**, 1701054.

16 J. B. Goodenough and Y. Kim, *Chem. Mater.*, 2010, **22**, 587–603.

17 J. A. Saint, M. M. Doeff and J. Wilcox, *Chem. Mater.*, 2008, **20**, 3404–3411.

18 J. Rodríguez-Carvajal, *Phys. B*, 1993, **192**, 55–69.

19 K. Momma and F. Izumi, *J. Appl. Crystallogr.*, 2011, **44**, 1272–1276.

20 Y. Cao, L. Xiao, W. Wang, D. Choi, Z. Nie, J. Yu, L. V. Saraf, Z. Yang and J. Liu, *Adv. Mater.*, 2011, **23**, 3155–3160.

21 K. Dai, J. Mao, X. Song, V. Battaglia and G. Liu, *J. Power Sources*, 2015, **285**, 161–168.

22 W. J. Shi, D. Zhang, X. M. Meng, C. X. Bao, S. D. Xu, L. Chen, X. M. Wang, S. B. Liu and Y. C. Wu, *ACS Appl. Mater. Interfaces*, 2020, **12**, 14174–14184.

23 Y. Wang, J. Liu, B. Lee, R. Qiao, Z. Yang, S. Xu, X. Yu, L. Gu, Y.-S. Hu, W. Yang, K. Kang, H. Li, X.-Q. Yang, L. Chen and X. Huang, *Nat. Commun.*, 2015, **6**, 6401.

24 Z. Liu, W. G. Lin, K. W. Zhou and J. L. Yan, *Ceram. Int.*, 2018, **44**, 2797–2802.

25 U. Dutta, D. Ghosh, A. Haque, P. S. Walke, N. E. Mordvinova, O. I. Lebedev, K. Pal, A. Gayen, A. K. Kundu and M. M. Seikh, *J. Magn. Magn. Mater.*, 2018, **464**, 132–138.

26 U. Rizal, S. Das, D. Kumar, B. S. Swain and B. P. Swain, *AIP Conf. Proc.*, 2016, **1724**, 020135.

27 Z. Xiao, F. Xia, L. Xu, X. Wang, J. Meng, H. Wang, X. Zhang, L. Geng, J. Wu and L. Mai, *Adv. Funct. Mater.*, 2022, **32**, 2108244.

28 Y. Zhang, H. Xie, H. Jin, X. Li, Q. Zhang, Y. Li, K. F. Li, F. Luo, W. Li and C. Li, *ACS Omega*, 2021, **6**, 21304–21315.

29 M. C. Biesinger, B. P. Payne, A. P. Grosvenor, L. W. M. Lau, A. R. Gerson and R. S. C. Smart, *Appl. Surf. Sci.*, 2011, **257**, 2717–2730.

30 M. C. Biesinger, L. W. M. Lau, A. R. Gerson and R. S. C. Smart, *Appl. Surf. Sci.*, 2010, **257**, 887–898.

31 Y.-U. Park, R. A. Shakoor, K.-Y. Park and K.-S. Kang, *J. Electrochem. Sci. Technol.*, 2011, **2**, 14–19.

32 Y. S. Lee and K. S. Ryu, *Sci. Rep.*, 2017, **7**, 16617.